Lifetimes in ^{15}N from gamma-ray line shapes produced in the ^{2}H(^{14}N, $p\gamma$) and ^{14}N(thermal n, γ) reactions

S. Raman,[1] E. T. Jurney,[2] J. W. Starner,[2] A. Kuronen,[3] J. Keinonen,[3] K. Nordlund,[3] and D. J. Millener[4]
[1]*Oak Ridge National Laboratory, Oak Ridge, Tennessee 37831*
[2]*Los Alamos National Laboratory, Los Alamos, New Mexico 87545*
[3]*Accelerator Laboratory, University of Helsinki, FIN-00014 Helsinki, Finland*
[4]*Brookhaven National Laboratory, Upton, New York 11973*
(Received 24 February 1994)

Mean lifetimes of bound states in ^{15}N were inferred from the Doppler-shift-attenuation (DSA) of γ rays produced in the inverse reaction ^{2}H(^{14}N, $p\gamma$) and from the primary gamma-ray-induced Doppler broadening (GRID) of secondary γ rays in the thermal-neutron capture reaction ^{14}N(n,γ). Targets for the DSA measurements were prepared by implanting first neon into a gold backing and then deuterium into the same region such that deuterium was trapped at the neon precipitates. To find out experimentally the initial velocity distributions of the recoiling ^{15}N nuclei, another target was prepared by implanting deuterium into silicon, which is a slow stopping-power medium. Computer simulations with the Monte Carlo method and experimental stopping powers were used in the DSA analysis of the γ-ray line shapes. This analysis yielded the following lifetimes for eight bound levels in ^{15}N: 43 $\pm$ 4 fs (5.30 MeV), $<$ 12 fs (6.32 MeV), 11 $\pm$ 2 fs (7.16 MeV), $<$ 3 fs (7.30 MeV), 129 $\pm$ 6 fs (7.57 MeV), $<$ 3 fs (8.31 MeV), $<$ 10 fs (8.57 MeV), and $<$ 4 fs (9.05 MeV). GRID measurements were made with melamine ($C_3H_6N_6$) and with silicon nitride (Si_3N_4) as both targets and slowing-down media. Measurements were also made with air (80% nitrogen). The Doppler-broadened γ-ray line shapes were analyzed by molecular-dynamics simulations of the slowing-down process to obtain the lifetime values of 40 $\pm$ 3 fs (5.30 MeV), $<$ 2 fs (6.32 MeV), $<$ 3 fs (7.30 MeV), and $<$ 3 fs (8.31 MeV) for levels in ^{15}N. The extent to which the mirror symmetry of levels in ^{15}N and ^{15}O is valid is examined in some detail.

PACS number(s): 21.10.Tg, 27.20.+n

I. INTRODUCTION

Considerable attention in the literature has been focused on the excited states of the mirror nuclei ^{15}N and ^{15}O because their lowest-order configurations in the shell model lack only a single nucleon to close the $1p$ shell. The mirror symmetry of states in these nuclei is illustrated in Fig. 13 of the compilation of Ajzenberg-Selove [1]. There are nine bound states in ^{15}N below the excitation energy of 9.1 MeV. The mean lifetimes (τ) of these states have been studied by (γ,γ), (e,e'), Doppler broadening, recoil distance, and Doppler-shift-attenuation (DSA) methods [2–17]. In most cases, the lifetimes adopted in Ref. [1] (see Table I) are based on measurements that are mutually inconsistent and carry large uncertainties. Details concerning previous DSA measurements are given in Table II. It is not surprising that the measured values show wide variations because a variety of targets with layered structures that make the DSA analysis complicated was used and because the stopping powers were in many cases small and poorly known. A systematic remeasurement of lifetimes of states in ^{15}N is therefore warranted.

The lifetimes of the first ($E_x = 5.27$ MeV), second (5.30 MeV), fourth (7.16 MeV), and sixth (7.57 MeV) levels in ^{15}N are in the 1 fs to 3 ps range accessible to the DSA method. In this work the improved DSA method developed at the Helsinki University Accelerator Laboratory [18] and the inverse reaction ^{2}H(^{14}N, $p\gamma$) were used to measure the lifetimes of the levels at E_x = 5.30, 7.16, and 7.57 MeV. Upper limits were also deduced for the lifetimes of the E_x = 6.32, 7.30, 8.31, 8.57, and 9.05 MeV levels known to have very short lifetimes of $<$ 3 fs [1]. Interference caused by the population of the 5.18- and 5.24-MeV levels in ^{15}O by the concurrent ^{2}H(^{14}N, $n\gamma$) reaction precluded an accurate DSA measurement of the lifetime of the 5.27-MeV level in ^{15}N.

In a separate experiment, the Doppler broadenings of the secondary γ rays from the levels at E_x = 5.30, 6.32, 7.30, and 8.31 MeV in ^{15}N—broadenings that result from nuclear recoil caused by the emission of primary γ rays to these levels in the ^{14}N(thermal n, γ) reaction—were studied at the Los Alamos Omega West Reactor. This type of experiment was first reported by Campbell, Harvey, and Slaughter [19] and independently (and in greater detail) by Wetzel [7]. Both studies involved the ^{14}N(n, γ) reaction. Wetzel's old gamma-ray-induced Doppler broadening (GRID) [20] measurements have been repeated here not only with a superior Ge detector and three different targets (melamine, silicon nitride, and air) but also with a sophisticated simulation of the Doppler-broadened γ-ray line shapes with a recently introduced molecular-dynamics (MD) simulation of the slowing down of atoms recoiling at ultralow velocities [21,22].

TABLE I. Lifetimes of levels in ^{15}N obtained in the current and previous works.

	Previous work			Ref. [1]	This work	
				Adopted value	^{2}H(^{14}N, $p\gamma$)	^{14}N(n,γ)
E_x(MeV)	τ(fs)[a]	Method[b]	Ref.	τ(fs)[a]	τ(fs)[a,c]	τ(fs)[a,d]
5.27	2900 *500*	Doppler shift attenuation	[2]	2580 *140*		
	2600 *200*	Doppler shift attenuation	[3]			
	2500 *500*	Doppler shift attenuation	[4]			
	2490 *240*	Recoil distance	[5]			
5.30	43 *18*	Doppler shift attenuation	[6]	25 *7*	43 *4*	40 *3*
	22 *7*	Doppler broadening	[7]			
6.32	< 45	Doppler shift attenuation	[8]	0.211 *12*	< 12	< 2
	< 29	Doppler shift attenuation	[9]			
	< 40	Doppler broadening	[7]			
	0.19 *4*	(e,e')	[10]			
	0.35 *7*	(e,e')	[11]			
	0.21 *2*	(γ,γ)	[12]			
	0.23 *2*	(γ,γ)	[13]			
	0.211 *12*	(γ,γ)	[14]			
7.16	115 *25*	Doppler shift attenuation	[15]	18 *8*	11 *2*	
	10 *2*	Doppler shift attenuation	[16]			
	28 *8*	Doppler shift attenuation	[4]			
	9 *7*	Doppler shift attenuation	[9]			
	< 18	Doppler shift attenuation	[8]			
7.30	< 25	Doppler shift attenuation	[8]	0.61 *5*	< 3	< 3
	< 50	Doppler shift attenuation	[4]			
	< 10	Doppler shift attenuation	[9]			
	< 30	Doppler broadening	[7]			
	0.25 *19*	(e,e')	[17]			
	0.61 *5*	(γ,γ)	[14]			
7.57	150 *50*	Doppler shift attenuation	[15]	12^{+11}_{-6}	129 *6*	
	60 *20*	Doppler shift attenuation	[8]			
	12^{+11}_{-6}	Doppler shift attenuation	[9]			
8.31	< 21	Doppler shift attenuation	[8]	1.7 *11*	< 3	< 3
	< 16	Doppler shift attenuation	[9]			
	< 20	Doppler broadening	[7]			
	1.7 *11*	(γ,γ)	[14]			
8.57	11 *7*	Doppler shift attenuation	[9]	0.7 *7*	< 10	
	0.7 *7*	(γ,γ)	[14]			
9.05	< 2	Doppler shift attenuation	[9]	0.50 *8*	< 4	
	0.50 *8*	(γ,γ)	[14]			

[a] In our notation, 2900 *500* ≡ 2900 ± 500, 2580 *140* ≡ 2580 ± 140, etc.

[b] For more experimental details of the Doppler shift attenuation measurements, see Table II.

[c] Corrected for feeding. Quoted uncertainties include also the uncertainty in the experimental stopping power.

[d] Quoted uncertainties include also a 1% uncertainty assigned to the fitted FWHM values of Table III.

TABLE II. Summary of DSA lifetime measurements of ^{15}N levels.

Ref.	Reaction	$v/c(\%)$	Slowing-down medium	DSA analysis
Current	$^{2}H(^{14}N, p)$	5.0	Au and implanted ^{20}Ne and ^{2}H	a
[2]	$^{2}H(^{14}N, p)$	5.0	$(CD_2)_n$ on thick Mg, Al, Cu, and Au backings	b
[2]	$^{9}Be(^{14}N,^{8}Be)$	6.0	Be on thick Mg, Al, Cu, and Au backings	b
[3]	$^{13}C(^{3}He, p)$	1.6	50–80 $\mu g/cm^2$ ^{13}C on Au (200 μm) and Fe (25 μm) backings	c
[4]	$^{13}C(^{14}N,^{15}N^*)$	2.5	20–30 $\mu g/cm^2$ ^{13}C on 0.2-mm-thick Ta and Ni backings	d
[6]	$^{3}H(^{16}O, \alpha)$	3.1	^{3}H absorbed in a 0.5-mg/cm^2 thick Ti layer deposited on a thick Ni backings	e
[8]	$^{2}H(^{14}N, p)$	5.1	^{2}H impregnated into 90- and 180-$\mu g/cm^2$ thick Ti evaporated onto Cu and Al backings	f
[9]	$^{12}C(^{7}Li, \alpha)$	3.4	83-$\mu g/cm^2$ thick evaporated C target	g
[15]	$^{13}C(^{3}He, p)$	1.1	30–40 $\mu g/cm^2$ ^{13}C on Pt	h
[16]	$^{14}C(p,\gamma)$			i

[a]Experimental stopping power. Computer simulation of the slowing down process.

[b]Energy loss calculated according to $-(dE/dx) = K_n(v_0/v) + K_e(v/v_0)$, where $v_0 \approx c/137$. Values of K_e were extrapolated from experimental data reported by D. I. Porat and K. Ramavataram, Proc. Roy. Soc. **A252**, 394 (1959); *ibid.* **A77**, 97 (1961); *ibid.* **A78**, 1135 (1961); and L. C. Northcliffe, Annu. Rev. Nucl. Sci. **13**, 67 (1963). The ratio K_e/K_n was extrapolated from data by P. G. Bizzetti, A. M. Bizzetti-Sona, G. Di. Caporiacco, and M. Mando, Nucl. Instrum. Methods **34**, 261 (1965) and by H. Morgenstern, D. Hilscher, and J. Scheer, *ibid.* **39**, 347 (1966). Change of the unshifted peak intensity as a function of characteristic slowing down time was used to deduce the lifetime value.

[c]Energy loss calculated from the LSS theory [J. Lindhard, M. Scharff, and H. E. Schiøtt, Mat. Fys. Medd. Dan. Vid. Selsk. **33**, No. 14 (1963)] with the large angle scattering corrections by A. E. Blaugrund, Nucl. Phys. **88**, 501 (1966). Electronic stopping power was multiplied by 0.95.

[d]Energy loss calculated according to $-(dE/dx) = K_n(v/v_0)^{-1} + K_e(v/v_0) - K_3(v/v_0)^3$. The coefficients were deduced from experimental range data measured for ^{15}N in Ni and Ta by P. H. Barker and W. R. Phillips, Proc. Phys. Soc. **86**, 379 (1965) and W. R. Phillips and F. H. Read, *ibid.* **81**, 1 (1963).

[e]Lifetime was deduced from $\tau = (v_0/a)(1-F)$, where F is the attenuation coefficient and a is another coefficient calculated from stopping power data by I. Grant, 1964, unpublished.

[f]Energy loss calculated by using proton stopping power data and an effective charge which is obtained by fitting a curve to the effective charges deduced from heavy-ion stopping data (see Ref. [8] for details).

[g]Stopping power from the LSS theory [J. Lindhard, M. Scharff, and H. E. Schiøtt, Mat. Fys. Medd. Dan. Vid. Selsk. **33**, No. 14 (1963)] with the large-angle scattering corrections of A. E. Blaugrund, Nucl. Phys. **88**, 501 (1966).

[h]Energy loss calculated as given in footnote b; K_n was obtained from a parametrization of the values calculated from the LSS theory.

[i]No information on the experimental details and DSA analysis is given.

II. EXPERIMENT

A. Reaction $^{2}H(^{14}N, p\gamma)^{15}N$

For the $^{2}H(^{14}N, p\gamma)$ reaction study, a 10-MeV $^{14}N^{3+}$ beam of about 30-particle nA was supplied by the 5-MV tandem accelerator EGP-10-II of the Helsinki University Accelerator laboratory. The beam energy was selected—by measuring the excitation function—to minimize the population [in the $^{2}H(^{14}N, n\gamma)$ reaction] of the analog states in ^{15}O whose decays produce γ rays that interfere in the DSA analysis of ^{15}N states. At $E(^{14}N) = 10$ MeV, the only analog states populated are those at 5.18 and 5.24 MeV. The beam spot was 2×2 mm^2 on the target.

The ^{2}H targets were prepared by first implanting 100-keV $^{20}Ne^+$ (3×10^{16} ions cm^{-2}) and then 25-keV $^{2}H^+$ (6×10^{17} ions cm^{-2}) into a 0.4-mm-thick gold foil with an isotope separator. The ^{20}Ne implantation was necessary to provide trapping sites for ^{2}H at the neon precipitates and thus to avoid the diffusion of ^{2}H in gold [23–25]. The vacancies produced in the ^{2}H implantation migrate to the neon-precipitate-gold interface and then effectively trap ^{2}H atoms [24]. A target was also prepared by implanting 15-keV $^{2}H^+$ (4×10^{18} ions cm^{-2}) into a 2-mm-thick high-purity crystalline silicon wafer.

During the measurements, the target was set perpendicular relative to the beam direction. The target holder, made of copper, was air cooled. A vacuum better than 2 μPa was maintained in the target chamber to minimize carbon buildup. The deposition of carbon was monitored continuously using the 1369-keV γ ray in ^{24}Mg from the reaction $^{12}C(^{14}N, pn\gamma)$.

The γ radiations resulting from target bombardment were detected by an escape-suppressed spectrometer (ESS) consisting of an ORTEC HPGe detector (with

40% efficiency) surrounded by a cylindrical (thickness 3.5 cm and length 20 cm) HARSHAW bismuth-germanate (BGO) veto detector. The escape (Compton) suppression factor was about 4. For γ-ray energies of 2, 4, and 6 MeV, the full width at half maximum (FWHM) values were 3.1, 4.4, and 5.5 keV, respectively. The spectra were stored in a 16384-channel memory with a dispersion of 0.66 keV/channel. Spectrometer stability was checked with a ^{208}Tl γ-ray source, the ^{40}K laboratory background, and the unshifted peaks from the decays of the long-lived 5.27-MeV (^{15}N, τ = 2.58 ps [1]) and 5.24-MeV (^{15}O, τ = 3.25 ps [1]) levels. Energy and efficiency calibrations were performed with ^{56}Co and ^{64}Ga sources [26] placed in the target position. The unshifted peaks were used also for internal calibration of energies above 4.8 MeV.

Doppler-shifted γ rays were detected at 0° relative to the incident beam. The detector was located 4.0 cm from the target, and a graded absorber (2 mm lead, 1 mm cadmium, and 1.5 mm copper) was used to reduce the counting rate due to low-energy γ rays and x rays.

B. Reaction ^{14}N(thermal n, γ)

The (n, γ) measurements were carried out in the thermal column of the internal-target facility at the Los Alamos Omega West Reactor. The bulk of the measurements were made with melamine ($C_3H_6N_6$) as target material. Some measurements were also made with silicon nitride (Si_3N_4) and with air (80% nitrogen). The Los Alamos facility and the data analysis procedures have been described in Ref. [27]. Gamma-ray spectra were obtained in the pair-spectrometer mode with a 30-cm^3 coaxial intrinsic Ge detector positioned inside a 20-cm-diam by 30-cm-long NaI(Tl) annulus. Spectra were accumulated in a 16 384-channel memory with a dispersion of 0.629 keV/channel. For γ-ray energies of 3, 5, 7, and 9 MeV, the FWHM values were 2.5, 3.3, 4.0, and 4.7 keV, respectively.

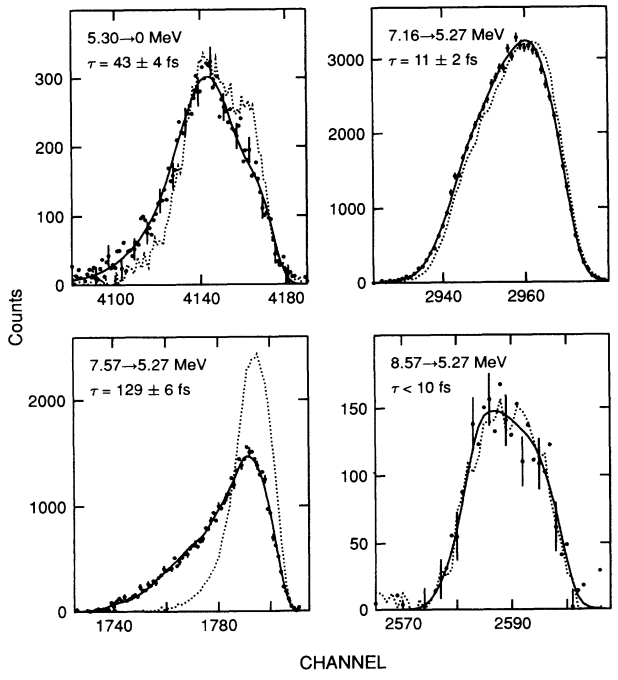

FIG. 1. Measured Doppler-broadened line shapes for selected transitions in ^{15}N observed at 0° in the ^{2}H(^{14}N, $p\gamma$) reaction with gold (dots) and silicon (dashed line) as slowing-down media. The dispersion is 1.32 keV/channel except for the transition 7.16 → 5.27 MeV where it is 0.66 keV/channel. The solid line is the Monte Carlo simulation of the γ-ray line shape. In the case of the 8.57-MeV level, a lifetime of 5 fs was used in the simulation. In other cases, the lifetime used is the one given in the figure.

III. RESULTS

A. Reaction ^{2}H(^{14}N, $p\gamma$)^{15}N

Figures 1 and 2 show the Doppler-shifted γ-ray peaks from the decays of several states in ^{15}N populated by the ^{2}H(^{14}N, $p\gamma$) reactions. Preliminary comparison of the line shapes observed with gold and silicon as slowing-down media revealed that the lifetime values could be deduced only for the E_x = 5.30, 7.16, and 7.57 MeV levels, whereas for the E_x = 6.32, 7.30, 8.31, 8.57, and 9.05 MeV levels only upper limits (based on the statistical uncertainties of the counts per channel) could be deduced. Figure 2 illustrates also the strong effects of the angular distribution of the emitted protons on the velocity distribution of the recoiling ^{15}N nuclides and thus on the observed γ-ray line shapes. The known lifetime 8.2 ± 1.0 fs [28] of the 5.18-MeV level in ^{15}O was used as a cross-check for the DSA measurements and analysis.

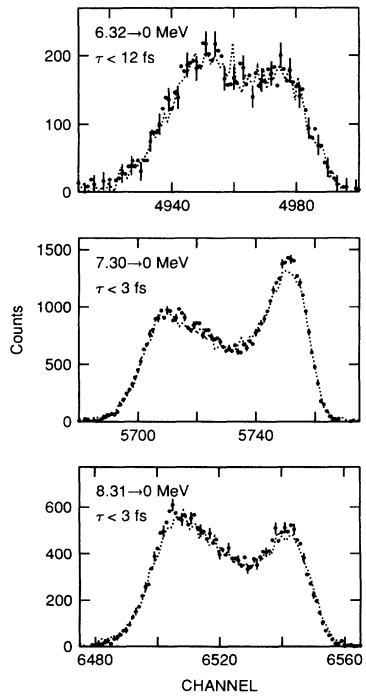

FIG. 2. Same as Fig. 1 for three additional transitions in ^{15}N. The dispersion is 1.32 keV/channel.

In the analysis of the measured γ-ray line shapes, the stopping power was described by

$$\left(\frac{dE}{dx}\right) = \left(\frac{dE}{dx}\right)_n^{\mathrm{ZBL}} + \left(\frac{dE}{dx}\right)_e^{\mathrm{expt}} . \quad (1)$$

The electronic stopping powers $(dE/dx)_e$ of gold and silicon for ^{15}N ions at $(0\text{–}6)v_0$ (where $v_0 \approx c/137$ is the Bohr velocity and c is the velocity of light in vacuum) were taken from Refs. [29] and [30], respectively. The uncertainty of the electronic stopping power was estimated as $\pm$ 5%. The electronic stopping power for ^{15}O ions was taken from Ref. [29]. The nuclear stopping power $(dE/dx)_n$ was calculated by the Monte Carlo (MC) method in which the scattering angles of the recoiling ions were directly derived from the classical scattering integral [31,30] and the interatomic interaction was described by the universal Ziegler-Biersack-Littmark (ZBL) potential [30]. In the cases studied here, where the recoil velocities are high and the states have short lifetimes, the nuclear stopping power has only a small effect on the line shapes.

Previous studies [32–34] on implanted targets indicate that the implanted layer has no significant effect on the density of gold and silicon probed by $v/c \approx 5\%$ ^{15}N recoils and, hence, on the extracted lifetimes.

The DSA analysis of the measured γ-ray line shape was performed by a computer simulation with the MC method [31,33,35]. For each case, a simulated line shape was obtained as the sum of the shapes corresponding to the direct (prompt) and cascade (delayed) feeding of the respective state. The sum was weighted by the experimental fractions of the feedings which were obtained from the extensively studied decay scheme of ^{15}N levels [1]. Attenuation of the observed Doppler shifts caused by the finite solid angle and by the finite initial velocity distribution of ^{15}N nuclei (resulting from the emission of protons) was estimated from the γ rays of short-lived states ($\tau < 15$ fs) measured with the implanted silicon backing, which represents a low stopping-power medium. In this case, the line shape is determined by the initial recoil velocity distribution and the detector geometry. When $\tau > 15$ fs, the initial velocity distribution has only a minor effect on the line shape and the two sets of data (with implanted Au and Si) were analyzed iteratively and in a self-consistent manner. The uncertainty in the lifetime values caused by the uncertainty of the initial velocity distribution was determined by varying the distribution in the range $\chi^2_{\min} - 1/N \leq \chi^2 \leq \chi^2_{\min} + 1/N$, where χ^2 is the goodness of the fit and N is the number of degrees of freedom in the fitting. The uncertainty was in all cases less than 2 fs. The measured dependence of the detector efficiency on the angle between the detector symmetry axis and the direction of γ-ray emission was taken into account.

The results are summarized in Table I. The lifetime value for the 7.57-MeV level adopted in Ref. [1] is taken from Ref. [9]. Because not enough details are given in Ref. [9] it is difficult to understand why the value obtained in Ref. [9] differs significantly from the current value. At any rate, the difference in line shapes for the 7.57→5.27-MeV transition (see the dotted and solid curves in Fig. 1) clearly establishes that the lifetime of the 7.57-MeV level is an order of magnitude larger than that given in Ref. [9].

B. Reaction ^{14}N(thermal n, γ)

Figure 3 shows a small portion of a typical spectrum obtained in the pair-spectrometer mode. The measured Gaussian FWHM values of the primary transitions (see the fourth column of Table III) were fitted with a polynomial of third order. The fitted values, given in the next column, represent the instrumental resolution. The measured FWHM values of five secondary transitions in ^{15}N (see the sixth column of Table III) are larger than the fitted values by an amount due to Doppler broadening. The accuracy with which this broadening can be measured does depend on the instrumental resolution, but the effect itself has been observed earlier with detection systems that possessed inferior resolution (see Fig. 4). At 6.3 MeV, the FWHM values were 4.7 and 5.6 keV in Refs. [7,19], respectively, compared to the 3.6 keV in the current work. To first order, it can be shown that the amount of the Doppler broadening is not strongly dependent on resolution.

In the thermal-neutron capture reaction on ^{14}N, the compound nucleus ^{15}N gets an excitation energy of 10.833 MeV and decays through γ-ray cascades to the ^{15}N ground state. Each time a γ ray is emitted, this process imparts a recoil velocity v to ^{15}N which results in a Doppler shift ΔE_γ of the *subsequent* γ ray E_γ. For example, in populating the 5.299- and 8.313-MeV levels, the primary 5.533- and 2.520-MeV γ rays produce recoil velocities of 120 and 50 km/s, respectively. The amount of Doppler shift will depend on the angle θ between the velocity vector of the recoiling nucleus and the direction of secondary γ-ray detection; that is, $\Delta E_\gamma = E_\gamma(v/c)\cos\theta$. The *maximum* Doppler shifts of the secondary 5.299- and 8.313-MeV transitions are 2.1 and 1.5 keV, respectively.

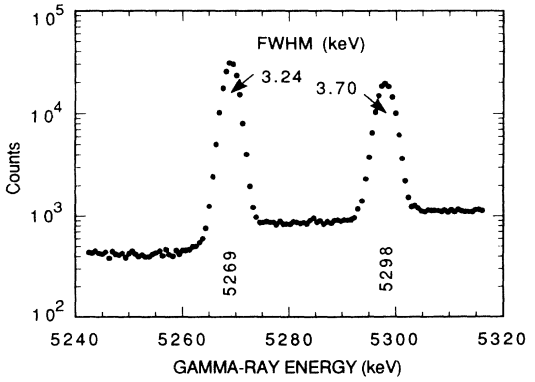

FIG. 3. Selected portion of the γ-ray spectrum from thermal-neutron capture by ^{14}N in melamine. The FWHM value for the 5.27-MeV peak is only 0.03 keV wider than the instrumental resolution, whereas that of the 5.30-MeV peak is 0.48 keV wider.

TABLE III. FWHM values of primary and secondary γ rays from the (n,γ) reaction. The capturing state is denoted by C. In our notation, 1.865 *20* ≡ 1.865 ± 0.020, etc. Certain secondary transitions in ^{15}N show clear evidence of significant Doppler broadening. The values listed in the last three columns were all obtained with melamine targets.

Final nucleus	E_γ (MeV)	Placement	FWHM (keV) Primary	Fitted	Secondary	Doppler broadening (keV) This work	Ref. [7]	Ref. [19]
^{2}H	2.223	C → 0	1.865 *20*	1.847				
^{15}N	2.520	C → 8.313	1.985 *14*	2.002				
^{15}N	3.532	C → 7.300	2.468 *21*	2.490				
^{15}N	3.678	C → 7.155	2.576 *15*	2.556				
^{15}N	4.509	C → 6.324	2.896 *27*	2.911				
^{13}C	4.945	C → 0	3.100 *19*	3.086				
^{15}N	5.269	5.270 → 0		3.212	3.239 *35*	0.027 *35*	0.08 *7*	
^{15}N	5.298	5.299 → 0		3.223	3.700 *25*	0.477 *25*	0.59 *7*	
^{15}N	5.533	C → 5.299	3.291 *19*	3.311				
^{15}N	5.562	C → 5.270	3.323 *23*	3.322				
^{3}H	6.250	C → 0	3.606 *49*	3.571				
^{15}N	6.322	6.324 → 0		3.596	4.467 *28*	0.871 *28*	0.84 *5*	0.9 *1*
^{15}N	7.299	7.301 → 0		3.930	4.595 *16*	0.665 *16*	0.65 *6*	
^{14}C	8.174	C → 0	4.200 *37*	4.217				
^{15}N	8.310	8.313 → 0		4.262	4.711 *18*	0.449 *18*	0.43 *5*	
^{15}N	10.833	C → 0	5.098 *51*	5.095				

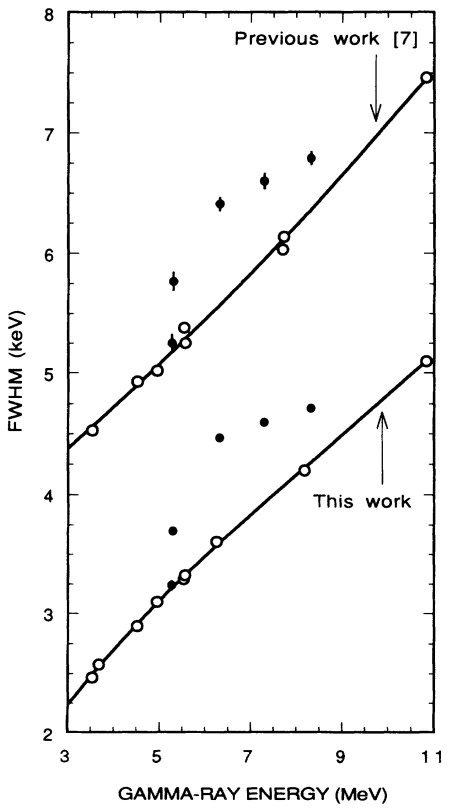

FIG. 4. Doppler broadening of secondary transitions in the ^{14}N(thermal n, γ) reaction with a melamine target. Solid lines denote instrumental resolution. Open and solid circles represent primary and secondary transitions, respectively.

In thermal-neutron capture, the primary γ rays (and the secondary ones) are emitted isotropically if the target nuclei are not aligned. Therefore, the Doppler effect will manifest itself as a broadening of the secondary peak. When the maximum Doppler shift is comparable to the energy resolution of a typical Ge detector—as it is in the case of ^{15}N—this broadening can be readily detected [36]. The amount of broadening depends on the velocity of the recoiling nuclei at the moment of γ-ray emission. In the analysis of the broadening, the velocity distribution can be connected to the lifetime of the relevant level if the initial recoil velocity, the lifetimes of the cascade-feeding levels, and the stopping power of the slowing-down material are known.

1. GRID analysis

To calculate the energy loss of atoms recoiling at very low velocities produced in primary γ-ray emissions, previous authors had used the binary collision approximation (BCA) in the framework of a Boltzmann transport equation [37] and a mean-free-path length approximation [38]. For the current application, both methods are inadequate representations of recoiling atoms in a realistic lattice. Moreover, the modeling should include not only elastic collisions of recoiling atoms with one constituent atom at a time but also interactions that involve more than one moderating atom. These collisions are simulated in this work by means of a constant energy and volume MD method [21,22] which directly connects the interatomic potential to the energy loss of a recoiling

atom in a realistic lattice.

In the simulations of the slowing down in melamine, the MD cell was comprised of 360 atoms, or 24 $C_3H_6N_6$ molecules. The molecules were assumed to be planar with bond lengths of 1.34 and 1.00 Å for the N–C and N–H bonds, respectively [39]. The crystal structure of melamine was assumed to be monoclinic with unit cell dimensions of 8.0, 6.9, and 2.4 Å corresponding to the density of 1.573 g/cm^3 [40].

In the simulations of the slowing down in silicon nitride (Si_3N_4), the MD cell had 244 atoms, or 8 unit cells of 28 atoms. The crystal structure was trigonal with a unit cell edge of 7.765 Å and an angle between unit cell edges of 60° [41].

In the simulations, one of the nitrogen atoms in the MD cell was given a recoil velocity in a random direction corresponding to the energy of the primary γ ray. Using the interatomic potentials given below, the velocity vector of the slowing-down atom was followed by numerically integrating the equations of motion for a time of typically 100 fs. The velocities of the recoiling atoms from about 1000 recoil events were used to construct the distribution of the recoil velocity as a function of time. From this distribution the γ-ray line shape was calculated [21] and convoluted with a Gaussian instrumental function.

In some cases, there is significant cascade feeding from the capturing state via intermediate states (see Table IV). In such cases the recoil velocity was given to the nitrogen atom in several steps, and the lifetimes of the intermediate states (see Table I) were taken into account. Different modes of populating a particular final state were selected at random according to the relative intensities given in Table IV.

TABLE IV. Direct and cascade feedings of the relevant levels in the $^{14}N(n,\gamma)$ reaction based on our unpublished measurements. The capturing state is denoted by C.

E_x (MeV)	Feeding	Intensity (%)
5.299	C → 5.299	91.8
	C → 9.222 → 5.299	0.2
	C → 9.155 → 5.299	3.8
	C → 8.313 → 5.299	3.0
	C → 7.301 → 5.299	1.1
	C → 6.324 → 5.299	0.1
6.324	C → 6.324	88.7
	C → 9.222 → 6.324	0.1
	C → 9.155 → 6.324	9.1
	C → 9.050 → 6.324	0.1
	C → 8.571 → 6.324	0.1
	C → 8.313 → 6.324	1.7
	C → 7.155 → 6.324	0.2
7.301	C → 7.301	91.9
	C → 8.313 → 7.301	1.4
	C → 9.155 → 7.301	6.7
8.313	C → 8.313	100

The interactions between the atoms in the MD cell were described by the repulsive ZBL pair potential [30]. An attractive potential was included to obtain the correct nearest-neighbor distances of the atoms. In simulations of melamine, a Morse potential [42] with a well depth of 2 eV was splined between $r = 0.5$ and 0.7 Å with the ZBL potential to get the correct bond lengths for the N–C and N–H bonds. In the case of silicon nitride, a Coulomb potential with effective charges of $+1.16e$ and $-1.55e$ for Si and N atoms, respectively, was added to the ZBL potential to reproduce the correct nearest-neighbor distances. The attractive potential was included only to prevent the crystal structure from breaking up during the simulations. The uncertainties in the parameters of the attractive potentials have negligible effect on the final results. Thermal displacements of the target atoms were neglected in the simulations.

The electronic stopping power, which is often ignored when the recoil velocities are very low ($\approx$ 100 km/s), was calculated by applying the Bragg law to the stopping cross sections [30] of individual elements of the target and included as a frictional force in the equations of motion of the recoiling ^{15}N atom. In the current case its inclusion has a non-negligible effect ($\approx$ 10%) on the final results.

2. *Level lifetimes*

The FWHM values of five secondary transitions in ^{15}N measured with the melamine target are shown in Fig. 5(a) together with the values calculated by the MD simulations for $\tau = 0.1$ fs. Also shown is the experimental resolution which represents an infinite lifetime.

The manner in which the Doppler broadening is related to the level lifetime is shown in Fig. 5(b), which shows the variations in the simulated FWHM values for selected lifetimes. In the 5–50 fs region, the recoiling nucleus is slowed down by the medium in such a way that the broadening is sensitive to the lifetime.

With respect to the direction in which the secondary γ rays are detected, the preceding primary γ rays have been emitted either isotropically or not—depending on the spins and mixing ratios that define the standard angular correlation between cascading γ rays. If the lifetime is so short that the recoiling nucleus has no chance to collide with nearby atoms (typically $\tau < 1$ fs in solids), any anisotropy present in the cascade will affect the observed broadening. If, as defined before, θ is the angle between the velocity vector of the recoiling nucleus and the direction of secondary γ-ray detection, the preceding primary transition was emitted in the direction $(\pi + \theta)$. The angular correlation between the primary and secondary transitions can be written as

$$W(\theta) \propto 1 + \alpha \cos^2 \theta, \tag{2}$$

where the coefficient α is defined by (a) the spins of the initial, intermediate, and final states and (b) the multi-

pole mixing ratios of the cascading transitions [43]. Figure 5(c) illustrates the extreme cases where $\alpha = +1$, $\alpha = 0$ (isotropic distribution), and $\alpha = -1$. Cascade feedings will dilute angular correlation effects because the net recoil velocity is the sum of the velocity vectors resulting from the preceding cascade transitions.

In melamine and silicon nitride, the recoiling ^{15}N nucleus will collide with another atom in about 1–3 fs. Once this happens, the emission direction of the secondary γ ray is no longer correlated to the recoil direction. If $\tau > 3$ fs, the bulk of the secondary γ-ray emissions will take place after the first collision, and the angular correlation will not affect the line shape which can now be approximated by the isotropic case. If $1 < \tau < 3$ fs, the line shape becomes complex—arising partly from emissions that take place before the first collision (during which angular correlation is important) and partly after (when it is not).

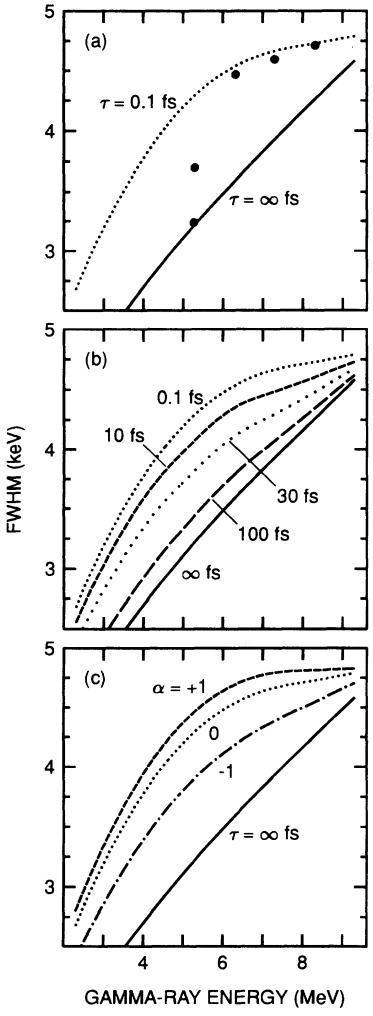

FIG. 5. (a) FWHM values of five secondary transitions measured in thermal-neutron capture by ^{14}N in melamine. They are bracketed by the MD simulations for $\tau = 0.1$ fs on the one side and by the instrumental resolution (the $\tau = \infty$ fs curve) on the other. (b) Sensitivity of the FWHM values to the level lifetime assuming zero angular correlations. (c) Sensitivity of the FWHM values to the angular correlations assuming $\tau = 0.1$ fs.

Because $J^\pi = 1^+$ for the ground state of ^{14}N, the J^π of the capturing state is a mixture of $\frac{1}{2}^+$ and $\frac{3}{2}^+$ states. For four transitions to the $\frac{1}{2}^-$ ground state of ^{15}N, the calculated FWHM values as a function of the lifetime are shown in Fig. 6 for melamine. It is again emphasized that certainly for $\tau < 1$ fs and, to a lesser extent, for $1 < \tau < 3$ fs, angular correlation effects, if allowed by the spins, are important.

The $J = \frac{1}{2}$ assignment [1] for the 5.30- and 8.31-MeV levels lead to $\alpha = 0$ in both cases, and the FWHM behaviors of their ground-state transitions are as shown in Figs. 6(a) and 6(d).

The mixing ratio for the $M1 + E2$ ground-state transition from the 6.32-MeV $J^\pi = \frac{3}{2}^-$ state is known to be $\delta_{\gamma_2} = +0.132 \pm 0.004$ [1] and the 4.51-MeV primary transition to this state from the $J^\pi = \frac{1}{2}^+ + \frac{3}{2}^+$ capturing state can be assumed to be nearly pure $E1$ ($\delta_{\gamma_1} \approx 0$). Hence, the effect of the angular correlation can be calculated for the extreme cases when the initial state is either pure $\frac{1}{2}^+$ or $\frac{3}{2}^+$. The resulting α values are $+0.207$ and -0.147, respectively, if the 6.32-MeV level were fed 100%

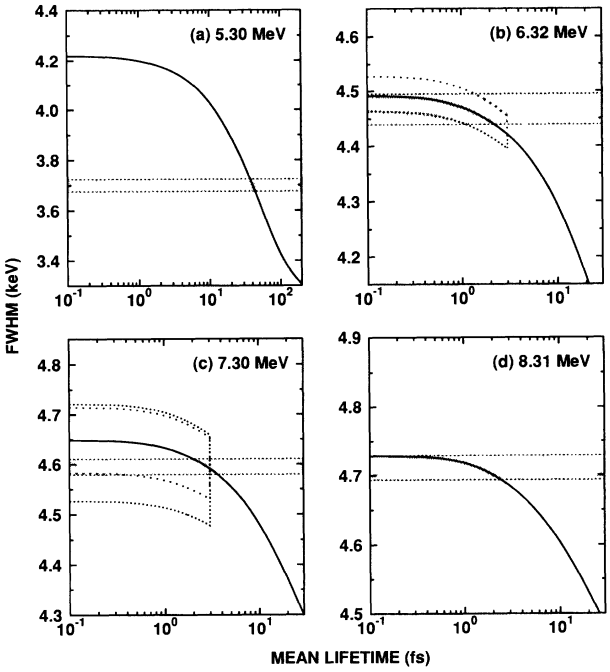

FIG. 6. Calculated FWHM values of four secondary transitions as a function of the level lifetimes. The recoiling nuclei are slowing down in melamine. The solid line corresponds to zero angular correlation. The measured FWHM value is shown by the shaded band. In the cases of the 5.30- and 8.31-MeV transitions, the measured FWHM values lead directly to lifetime values because angular correlation is not a factor in either case. In the cases of the 6.32- and 7.30-MeV transitions, their known mixing ratios together with the additional assumptions restrict the calculated FWHM values to the dotted region, as shown in (b) and (c), respectively. The spin sequences and the mixing ratios are discussed in Sec. III B 2.

by the 4.51-MeV transitions (no cascade feeding), but because it is not, these values need to be multiplied by the direct fraction of the population (see Table IV). The resulting α values are +0.184 and −0.131, respectively. The corresponding behaviors of the simulated FWHM values are shown in Fig. 6(b).

In the case of the 7.30-MeV, $J^\pi = \frac{3}{2}^+$ state, the ground-state transition is known to be nearly pure $E1$ from $\delta_{\gamma_2} = -0.017^{+0.005}_{-0.008}$ [1] but both the mixing ratio of the 3.53-MeV primary transition to this state and the spin composition of the initial capturing state are unknown. Therefore, the calculated extreme range of the FWHM values is very wide for lifetimes shorter than 3 fs as shown in Fig. 6(c). The extreme values correspond to cascade-feeding-corrected α values of −0.558 ($\frac{3}{2} \rightarrow \frac{3}{2} \rightarrow \frac{1}{2}$, $\delta_{\gamma_1} = -0.775$), −0.335 ($\frac{1}{2} \rightarrow \frac{3}{2} \rightarrow \frac{1}{2}$, $\delta_{\gamma_1} = -4.826$), +0.442 ($\frac{1}{2} \rightarrow \frac{3}{2} \rightarrow \frac{1}{2}$, $\delta_{\gamma_1} = +0.207$), and +0.495 ($\frac{3}{2} \rightarrow \frac{3}{2} \rightarrow \frac{1}{2}$, $\delta_{\gamma_1} = +1.291$).

From Fig. 6, it can be inferred that the experimental FWHM values of 3.700, 4.467, 4.595, and 4.711 keV (see Table III) correspond to the lifetimes of 40 ± 3 fs ($E_x = 5.30$ MeV), < 3 fs (6.32 MeV), < 4 fs (7.30 MeV), and < 3 fs (8.31 MeV), respectively, if the angular correlation effects are not taken into account. However, from the previous discussion, it can be seen that angular correlations have a significant effect on the lifetime results in the case of the 6.32- and 7.30-MeV levels.

To get information about the most probable values of α [see Eq. (2)], measurements were performed using an air target where the recoil can be assumed to move without slowing down appreciably. For the 6.32- and 7.30-MeV levels, the measured FWHM values (see Table V) were consistent with $\alpha = -0.131$ and $\alpha = -0.17 \pm 0.16$, respectively. Using these values of α, the melamine data yielded the lifetime limits of < 2 fs and < 4 fs for the 6.32- and 7.30-MeV levels, respectively.

The analysis of the FWHM values of 3.744, 4.475, 4.738, and 4.841 keV (see Table V) measured with the silicon nitride target yielded, without the angular correlation effects, the lifetime values of 40 ± 3 fs ($E_x = 5.30$ MeV), < 5 fs (6.32 MeV), < 3 fs (7.30 MeV), and < 3 fs (8.31 MeV), respectively, in fairly good agreement with the values obtained with the melamine target. When the α values obtained from the air target measurements were included in the analysis, the lifetime limits for the 6.32- and 7.30-MeV levels were not reduced significantly.

After combining the results of all three measurements, the final GRID lifetimes are given in Table I. For the 5.30-MeV level, the extracted lifetime of 40 ± 3 fs from the GRID measurement is in excellent agreement with the 43 ± 4 fs from the DSA measurement. This consistency shows that the potentials used give the correct stopping power. The GRID upper limits on the lifetimes for the 6.32-, 7.30-, and 8.31-MeV levels are also consistent with the current DSA values.

IV. MIRROR SYMMETRY OF ^{15}N AND ^{15}O

The current lifetimes for the 5.30-, 7.16-, and 7.57-MeV levels in ^{15}N are significantly different from those adopted in Ref. [1]. With the new lifetimes, the extent to which the mirror (isospin) symmetry of levels in ^{15}N and ^{15}O is valid can now be further examined. To this end, the lifetimes (converted to widths), γ-ray branching ratios, and resulting electromagnetic transition strengths for the nine lowest analog states are compared in Table VI. Apart from the lifetimes referred to above and the branching ratios for the 8.31-, 8.57-, and 9.05-MeV levels of ^{15}N (see Appendix A), the experimental information is taken from Ref. [1]. The lifetimes for the bound levels of ^{15}O adopted in Ref. [1] are mainly from previous DSA measurements carried out at the University of Helsinki [28]. The DSA analysis used experimental slowing-down data measured under similar conditions. Therefore the deduced lifetimes are insensitive to newer developments in stopping-power theory. The γ-ray widths of the three unbound levels of ^{15}O (above 7.30 MeV) included in Table VI are from the work of Schröder *et al.* [44]. The transition strengths have been derived from the data using the definitions of Weisskopf units (W.u.) given by Skorka *et al.* [45]. The ground-state (g.s.) $E2$ and $E3$ transition strengths in Table VI are derived from mixing ratios [1] or, in the case of the $\frac{7}{2}^+$ state, from small γ branches with large uncertainties.

For ^{15}N, inelastic electron scattering provides transition strengths with comparable or better precision (albeit with some model dependence if form factors are not measured at sufficiently low momentum transfers). An intercomparison is made in columns 5 and 6 of Table

TABLE V. FWHM values of secondary γ rays from the ^{14}N(n,γ) reaction obtained with melmine, silicon nitride (Si_3N_4), and air as targets. The instrumental resolution was obtained in each case by fitting a third order polynomial to the FWHM values of the primary transitions which are unbroadened. In our notation, 3.239 *35* ≡ 3.239 ± 0.035, etc.

E_γ	FWHM (keV)		FWHM (keV)		FWHM (keV)	
(MeV)	Instrumental	Melamine	Instrumental	Si_3N_4	Instrumental	Air
5.269	3.212	3.239 *35*	3.316	3.345 *16*	3.387	4.075 *16*
5.298	3.223	3.700 *25*	3.327	3.744 *20*	3.399	4.367 *39*
6.322	3.596	4.467 *28*	3.707	4.475 *30*	3.816	4.568 *25*
7.299	3.929	4.595 *16*	4.049	4.738 *41*	4.198	4.849 *33*
8.310	4.262	4.711 *18*	4.391	4.841 *47*	4.590	5.090 *59*

TABLE VI. Strengths, $B(\lambda)\downarrow$(W.u.), of electromagnetic transitions (between initial states i and final states f) in ^{15}N and ^{15}O for the nine lowest analog states. The radiation widths (Γ_γ) for the 5.30-, 7.16-, and 7.57-MeV levels in ^{15}N are from this work; all other data including spin and parity (J^π) assignments, branchings, and mixing ratios are from Ref. [1] except for slight modifications of some branching ratios as discussed in Sec. IV and Appendix A. In ^{15}O, levels above 7.30 MeV are (proton) unbound. In our notation, 2.55 *14* ≡ 2.55 ± 0.14, 0.69 *4* ≡ 0.69 ± 0.04, etc.

E_i(MeV)		J_i^π	Γ_γ(eV)		E_f(MeV)		J_f^π	Branching (%)		λ	$B(\lambda)\downarrow$(W.u.)	
^{15}N	^{15}O		^{15}N	^{15}O	^{15}N	^{15}O		^{15}N	^{15}O		^{15}N	^{15}O
5.27	5.24	$\frac{5}{2}^+$	(2.55 *14*)×10^{-4}	(2.03 *19*)×10^{-4}	0	0	$\frac{1}{2}^-$	100	100	*M*2+	0.69 *4*	0.57 *5*
										*E*3	7.5 *15*	3.7 *29*
5.30	5.18	$\frac{1}{2}^+$	(1.61 *12*)×10^{-2}	(8.0 *10*)×10^{-2}	0	0	$\frac{1}{2}^-$	100	100	*E*1	(2.6 *2*)×10^{-4}	(14 *2*)×10^{-4}
6.32	6.18	$\frac{3}{2}^-$	3.12 *18*	> 0.26	0	0	$\frac{1}{2}^-$	100	100	*M*1+	0.59 *3*	> 0.05
										*E*2	3.0 *3*	> 0.22
					5.27	5.24	$\frac{5}{2}^+$	< 0.1	< 2.5	*E*1	< 3.5×10^{-3}	
					5.30	5.18	$\frac{1}{2}^+$	< 0.05	< 2.5	*E*1	< 8.4×10^{-3}	
7.16	6.86	$\frac{5}{2}^+$	(6.0 *11*)×10^{-2}	(4.1 *7*)×10^{-2}	5.27	5.24	$\frac{5}{2}^+$	100	100	*M*1	0.43 *8*	0.47 *7*
7.30	6.79	$\frac{3}{2}^+$	1.09 *8*	> 0.023	0	0	$\frac{1}{2}^-$	99.3 *7*	100	*E*1+	(6.7 *6*)×10^{-3}	> 1.8×10^{-4}
										*M*2	0.17^{+11}_{-12}	≥ 0
					5.27	5.24	$\frac{5}{2}^+$	0.6 *1*		*M*1	0.038 *7*	
					5.30	5.18	$\frac{1}{2}^+$	0.2 *1*		*M*1	0.013 *7*	
7.57	7.28	$\frac{7}{2}^+$	(51 *3*)×10^{-4}	(9.4 *20*)×10^{-4}	0	0	$\frac{1}{2}^-$	1.3 *6*	3.8 *12*	*E*3	9 *4*	6.6 *25*
					5.27	5.24	$\frac{5}{2}^+$	98.7 *10*	96.2 *12*	*M*1	0.020 *1*	0.0052 *11*
8.31	7.56	$\frac{1}{2}^+$	0.37 *25*	0.042 *3*	0	0	$\frac{1}{2}^-$	81.1 *17*	3.5 *5*	*E*1	(1.3 *9*)×10^{-3}	(8.3 *13*)×10^{-6}
					5.30	5.18	$\frac{1}{2}^+$	10.9 *11*	15.8 *6*	*M*1	0.07 *5*	0.024 *2*
					6.32	6.18	$\frac{3}{2}^-$	5.2 *14*	57.5 *4*	*E*1	(6 *4*)×10^{-3}	(22 *2*)×10^{-3}
					7.30	6.79	$\frac{3}{2}^+$	2.8 *10*	23.2 *6*	*M*1	0.5 *4*	1.1 *1*
8.57	8.28	$\frac{3}{2}^+$	0.9 *9*	0.46 *6*	0	0	$\frac{1}{2}^-$	32.6 *16*	53.2 *3*	*E*1+	(1.2 *12*)×10^{-3}	(1.1 *2*)×10^{-3}
										*M*2	0.5 *5*	
					5.27	5.24	$\frac{5}{2}^+$	61.9 *16*	42.2 *5*	*M*1+	0.8 *8*	0.34 *4*
										*E*2	7 *7*	
					5.30	5.18	$\frac{1}{2}^+$		1.2 *1*	*M*1		0.0090 *14*
					6.32	6.18	$\frac{3}{2}^-$	1.8 *7*	2.2 *6*	*E*1	(4 *4*)×10^{-3}	(2.6 *8*)×10^{-3}
					7.16	6.86	$\frac{5}{2}^+$	3.6 *5*	1.2 *3*	*M*1	0.6 *6*	0.09 *3*
9.05	8.74	$\frac{1}{2}^+$	1.30 *22*	0.28 *6*	0	0	$\frac{1}{2}^-$	92.0 *9*		*E*1	(3.9 *7*)×10^{-3}	
					5.30	5.18	$\frac{1}{2}^+$	4.2 *5*	64 *3*	*M*1	0.050 *10*	0.19 *4*
					6.32	6.18	$\frac{3}{2}^-$	3.8 *5*	36 *3*	*E*1	(6.0 13)×10^{-3}	(15 *4*)×10^{-3}

VII. Furthermore, if ratios of π^+ to π^- inelastic scattering cross sections on ^{15}N near the delta-resonance energy are available, it is possible, with rather more model dependence, to relate transition strengths in ^{15}O to those in ^{15}N. The results of such an analysis are also given in Table VII. The sources of the (e,e') and (π,π') data and an outline of the analysis which leads to these results are given in Appendix B. For the 6.32- and 5.27-MeV levels in ^{15}N, the $B(E\lambda)$ values are in good agreement with those extracted from the lifetimes and mixing ratios. The value for the 7.57-MeV level is also in agreement, but it is much more precise. There are no γ-ray data on the weak g.s. $E3$ transition from the 7.16-MeV level.

If mirror symmetry holds for ^{15}N and ^{15}O, the expectation is that $E1$ transition strengths for analog transitions should be identical (see Table VI). However, the g.s. $E1$ strengths from the first $\frac{1}{2}^+$ ($\frac{1}{2}^+_1$) states, for which the lifetimes are accurately known, clearly violate mirror symmetry because the transition strength is ~ 5 times weaker in ^{15}N than in ^{15}O. Even larger violations are evident for the next two $\frac{1}{2}^+$ states. The g.s. $E1$ transitions are very weak in ^{15}O; it is 8×10^{-6} W.u. for the $\frac{1}{2}^+_2$ state, and even a 5% branch for the unobserved g.s. transition from the $\frac{1}{2}^+_3$ state would correspond to a transition strength of only 5×10^{-5} W.u.

The strengths of moderately strong $E2$ and $E3$ transitions in ^{15}N and ^{15}O are not expected to differ by large factors because the matrix elements are expected to be dominantly isoscalar in nature. Similar expectations hold for moderately strong $M1$ and $M2$ transitions, in which the isovector spin contributions are expected to dominate. As can be seen from Table VI, these general expectations hold quite well. In the following subsection, theoretical calculations for the structure of the states listed in that table are reviewed, and some predictions for transition rates are compared with experiment. Then, in the subsequent subsection, possible reasons for the breakdown in mirror symmetry for $E1$ transition strengths are discussed.

A. Shell-model calculations

Shell-model calculations for the positive-parity states, which require a basis of one-particle–two-hole ($1p2h$) and $3p4h$ configurations to account for the levels of interest, are described in detail by Alburger and Millener [46], who also discuss earlier calculations. Of the positive-parity levels listed in Table VI, only the 9.05-MeV, $\frac{1}{2}^+$ state has a shell-model counterpart which is mainly $3p4h$, although a substantial $3p4h$ component is predicted for the 8.57-MeV, $\frac{3}{2}^+$ state. The $\frac{7}{2}^+_1$ model state, identified with the 7.57-MeV level of ^{15}N and not listed in Table III of Ref. [46], is 97% $1p2h$ with a dominant ($\sim 80\%$) ^{14}N(g.s.)$\times d_{5/2}$ component. A number of arguments supporting the essential features of the predicted shell-model structure was given in Ref. [46]. Further evidence, which is relevant to our discussion of $E1$ transition strengths in the following subsection, comes from the excitation energy differences of the states in ^{15}N and ^{15}O resulting from Coulomb effects. Specifically, the rather different Coulomb energies of the active $0p$, $0d$, and $1s$ orbits, which decrease in the order given from roughly 3.5 MeV in steps of 300–400 keV, provide a sensitive test of configurational structure. The largest energy shift of 756 keV occurs for the 8.31-MeV, $\frac{1}{2}^+$ state, which has a rather pure ^{14}N(g.s.)$\times 1s_{1/2}$ configuration [46], and reflects the difference in Coulomb energies of the $0p$ and $1s$ orbits. A large shift of 508 keV also occurs for the 7.30-MeV, $\frac{3}{2}^+$ state, which has a large component of the same configuration. The 7.57-MeV, $\frac{7}{2}^+$ and 7.16-MeV, $\frac{5}{2}^+$ states, which have large ^{14}N(g.s.)$\times d_{5/2}$ components, have shifts just under 300 keV representing a substantial part of the difference in Coulomb energies of the $0p$ and $0d$ orbits. The 5.27-MeV, $\frac{5}{2}^+$ and 5.30-MeV, $\frac{1}{2}^+$ states, on the other hand, undergo small energy shifts of 29 and 116 keV, respectively. These states are predominantly $1p2h$ in nature with a greater $0d_{5/2}$ or $1s_{1/2}$ parentage to $T = 1$ than to $T = 0$ $2h$ states [46]; this finding translates into

TABLE VII. Comparison of $B(E2)$ and $B(E3)$ strengths (in W.u.) in ^{15}N and ^{15}O for transitions to the ground states from excited states denoted by E_x. The listed values are from electromagnetic data (see Table VI) and from analyses of electron and pion inelstic scattering on ^{15}N. In our notation, 7.5 *15* ≡ 7.5 ± 1.5, 1.06 *10* ≡ 1.06 ± 0.10, etc. The uncertainties given in columns 6, 7, and 9 are purely statistical. In particular, those in column 9 do not take into account any model dependence in the result (see Sec. IV).

^{15}N E_x(MeV)	^{15}O E_x(MeV)	J^π	λ	^{15}N $B(\lambda)\downarrow$ from Table VI	^{15}N $B(\lambda)\downarrow$ from (e,e')	^{15}N $\sigma(\pi^+)/\sigma(\pi^-)$ See Appendix B	^{15}O $B(\lambda)\downarrow$ from Table VI	^{15}O $B(\lambda)\downarrow$ See Appendix B
5.27	5.24	$\frac{5}{2}^+$	$E3$	7.5 *15*	7.8 *13*	1.06 *10*	3.7 *29*	6.9 *18*
6.32	6.18	$\frac{3}{2}^-$	$E2$	3.0 *3*	3.15 *12*	1.54 *20*	> 0.22	1.3 *4*
7.16	6.86	$\frac{5}{2}^+$	$E3$		0.30 *3*			
7.57	7.28	$\frac{7}{2}^+$	$E3$	9 *4*	3.7 *2*	0.57 *4*	6.6 *25*	11.5 *18*

roughly equal parentages of a neutron and a proton coupled to a p-shell core. Thus, the Coulomb-energy shifts of these two states are typical of the p shell.

A similar shell-model calculation, in which the $2\hbar\omega$ basis is truncated to states of high spatial and SU(3) symmetry, has been performed for the negative-parity states. In each calculation, the only adjustable parameter is a small energy shift applied to either the $3p4h$ or the $2p3h$ basis states to bring the final excitation energies of such states into good correspondence with experimental counterparts. The $1h$ intensities in the lowest $\frac{1}{2}^-$ and $\frac{3}{2}^-$ states of the $(0+2)\hbar\omega$ calculation are 88.2% and 78.1%, respectively.

A comparison of calculated and experimental electromagnetic transition strengths using wave functions from the calculations described above is given in Table VIII. The $M1$ strengths are a useful indicator of configuration

TABLE VIII. Experimental transition strengths in ^{15}N and ^{15}O (see Tables VI and VII) compared to shell-model values. In most cases, the wave functions are from truncated $(0+2)\hbar\omega$ and $(1+3)\hbar\omega$ calculations. For the cases marked by asterisks, only $1\hbar\omega \rightarrow 0\hbar\omega$ results are available. In a few cases, certain transition rates involving the final $\frac{5}{2}^+$ states at 5.27(^{15}N) and 5.24(^{15}O) MeV are not calculated. The harmonic oscillator wave functions used correspond to a length parameter $b = 1.687$ fm. Bare nucleon charges and g factors are used except for $E2$ and $E3$ transitions for which we used isoscalar and isovector effective charges $(1+\delta e_p + \delta e_n, 1+\delta e_p - \delta e_n)$ that equalled (2.0, 0.7) and (1.5, 0.77), respectively. In our notation, 0.69 *4* ≡ 0.69 ± 0.04, 0.57 *5* ≡ 0.57 ± 0.05, etc.

E_i(MeV)		J_i^π	E_f(MeV)		J_f^π	λ	$B(\lambda)\downarrow$(W.u.)(Theory)		$B(\lambda)\downarrow$(W.u.)(Experiment)	
^{15}N	^{15}O		^{15}N	^{15}O			^{15}N	^{15}O	^{15}N	^{15}O
5.27	5.24	$\frac{5}{2}^+$	0	0	$\frac{1}{2}^-$	$M2^*$ +	1.32	0.98	0.69 *4*	0.57 *5*
						$E3^*$	8.7	9.0	7.8 *13*	6.9 *18*
5.30	5.18	$\frac{1}{2}^+$	0	0	$\frac{1}{2}^-$	$E1$	1.3×10^{-4}	1.3×10^{-4}	$(2.6\ 2)\times10^{-4}$	$(14\ 2)\times10^{-4}$
6.32	6.18	$\frac{3}{2}^-$	0	0	$\frac{1}{2}^-$	$M1$ +	0.92	0.64	0.59 *3*	> 0.05
						$E2$	3.1	0.96	3.15 *12*	1.3 *4*
			5.30	5.18	$\frac{1}{2}^+$	$E1$	12×10^{-3}	12×10^{-3}	$<8.4\times10^{-3}$	
7.16	6.86	$\frac{5}{2}^+$	5.27	5.24	$\frac{5}{2}^+$	$M1$	0.53	0.45	0.43 *8*	0.47 *7*
7.30	6.79	$\frac{3}{2}^+$	0	0	$\frac{1}{2}^-$	$E1$ +	6.2×10^{-3}	6.2×10^{-3}	$(6.7\ 6)\times10^{-3}$	$>1.8\times10^{-4}$
						$M2$	3.7×10^{-4}	130×10^{-4}	0.17^{+11}_{-12}	
			5.30	5.18	$\frac{1}{2}^+$	$M1$	2.3×10^{-3}	1.5×10^{-3}	$(13\ 7)\times10^{-3}$	
7.57	7.28	$\frac{7}{2}^+$	0	0	$\frac{1}{2}^-$	$E3^*$	3.7	9.7	3.7 *2*	11.5 *18*
8.31	7.56	$\frac{1}{2}^+$	0	0	$\frac{1}{2}^-$	$E1$	1.1×10^{-3}	1.1×10^{-3}	$(1.3\ 9)\times10^{-3}$	$(8.3\ 13)\times10^{-6}$
			5.30	5.18	$\frac{1}{2}^+$	$M1$	0.039	0.032	0.07 *5*	0.024 *2*
			6.32	6.18	$\frac{3}{2}^-$	$E1$	0.43×10^{-3}	0.21×10^{-3}	$(6\ 4)\times10^{-3}$	$(22\ 2)\times10^{-3}$
			7.30	6.79	$\frac{3}{2}^+$	$M1$	0.36	0.70	0.5 *4*	1.1 *1*
8.57	8.28	$\frac{3}{2}^+$	0	0	$\frac{1}{2}^-$	$E1$ +	1.6×10^{-3}	1.6×10^{-3}	$(1.2\ 12)\times10^{-3}$	$(1.1\ 2)\times10^{-3}$
						$M2$	0.42	0.83	0.5 *5*	
			5.30	5.18	$\frac{1}{2}^+$	$M1$	1.9×10^{-4}	0.31×10^{-4}		$(90\ 14)\times10^{-4}$
			6.32	6.18	$\frac{3}{2}^-$	$E1$	2.5×10^{-3}	2.5×10^{-3}	$(4\ 4)\times10^{-3}$	$(2.6\ 8)\times10^{-3}$
9.05	8.74	$\frac{1}{2}^+$	0	0	$\frac{1}{2}^-$	$E1$	2.5×10^{-3}	2.5×10^{-3}	$(3.9\ 7)\times10^{-3}$	
			5.30	5.18	$\frac{1}{2}^+$	$M1$	0.087	0.072	0.050 *10*	0.19 *4*
			6.32	6.18	$\frac{3}{2}^-$	$E1$	1.1×10^{-3}	1.1×10^{-3}	$(6.0\ 13)\times10^{-3}$	$(15\ 4)\times10^{-3}$

mixing because the $M1$ operator does not connect states that differ in $\hbar\omega$. In this connection it can be seen that, except for two very weak transitions, theory and experiment are in rather good accord, even for the $\frac{1}{2}^+_3 \rightarrow \frac{1}{2}^+_1$ transition connecting states whose dominant components differ in oscillator quantum number (the same is true for the similar case, not shown in Table VIII, of $M1$ transitions from the $\frac{5}{2}^+_3$ state to the lower $\frac{5}{2}^+$ states). For the g.s. transitions from the $\frac{5}{2}^+_1$ and $\frac{7}{2}^+_1$ states, only results from a $1\hbar\omega \rightarrow 0\hbar\omega$ calculation are available. The $E3$ effective charges $1+\delta e_p+\delta e_n = 1.5$ and $1+\delta e_p-\delta e_n = 0.77$ are close to the values required to describe $E3$ transition rates in ^{13}C [47] and are typical of the values required for $E3$ transitions in $1\hbar\omega \rightarrow 0\hbar\omega$ calculations in this mass region. The overall reproduction of the $E3$ strengths (very sensitive to the value of the oscillator parameter) is good as are the predictions of a dominantly isoscalar transition from the $\frac{5}{2}^+_1$ state and a substantial isovector contribution to the decay of the $\frac{7}{2}^+_1$ state. The prediction of a substantial $M2$ strength in the decay of the $\frac{5}{2}^+_1$ state is also borne out, and the overprediction is typical of a $1\hbar\omega \rightarrow 0\hbar\omega$ calculation.

The $M1$ strength for the $\frac{3}{2}^- \rightarrow \frac{1}{2}^-$ transition is overpredicted and close to the value of 0.935 W.u. for pure $1h$ states [a consequence of the truncation of the $2\hbar\omega$ basis to configurations with high spatial and SU(3) symmetry]. About half the required reduction of the $M1$ matrix element can be achieved by the inclusion of core polarization, isobar currents, and meson-exchange currents [48]. The isoscalar effective charge $1 + \delta e_p + \delta e_n = 2.0$ required to get reasonable agreement with the experimental $B(E2)$ strengths for the same transition is larger than the value required for ^{13}C [47] and for many other p-shell nuclei, but it is more consistent with the larger values required at and close to ^{16}O.

B. Electric-dipole transitions

The predicted g.s. $E1$ strengths are in surprisingly good agreement with the experiment for ^{15}N, as was noted in Ref. [14]. In view of the strong violations of isospin symmetry evident in the comparison of mirror $E1$ transition strengths, this agreement may be fortuitous. The predictions for $E1$ transitions in ^{15}N which involve the $\frac{3}{2}^-$ final state are not so successful.

The $E1$ transition strengths are weak, and the theoretical matrix elements involve considerable cancellation among contributions from different pairs of orbits. In this situation, the use of more realistic single-particle wave functions in the place of harmonic oscillator wave functions can sometimes make a significant change in the transition strength. In particular, if an orbit — especially a $1s$ orbit — is rather loosely bound, this mechanism can explain both abnormally large $B(E1)$ values for transitions between low-lying states [49] and differences in the strengths of mirror $E1$ transitions. However, for ^{15}N and ^{15}O, changes in the radial wave functions alone are unlikely to be able to account for the factor of 5 difference in the $\frac{1}{2}^+_1 \rightarrow \frac{1}{2}^-_1$ strengths because the separation energies for nucleons are not particularly low and because there is also strong cancellation of the $1s_{1/2} \rightarrow 0p_{1/2}$ and $1s_{1/2} \rightarrow 0p_{3/2}$ contributions to the $E1$ matrix element which lessens the sensitivity to changes in the $1s$ radial wave function.

Another mechanism for producing a difference in mirror transition strengths is suggested by the rather large differences in Coulomb energy shifts for different configurations. The inclusion of the single-particle Coulomb energy shifts in the shell-model calculation would lead to the diagonalization of different energy matrices for ^{15}N and ^{15}O. The consequent changes in wave functions could substantially alter $E1$ matrix elements and thus lead to a breakdown of mirror symmetry. Such a mechanism has been suggested as a contributor to the mirror asymmetry of the $\frac{1}{2}^+_1 \rightarrow \frac{1}{2}^-_1$ transitions in ^{13}C and ^{13}N [50] (also, in this case, nucleon separation energies are low and different in the two nuclei). Even the simplest estimate suggests about a 1.5% difference in the $3p4h$ admixtures in the lowest $\frac{1}{2}^+$ states of ^{15}N and ^{15}O, and changes within the $1p2h$ part of the wave functions are also expected. The possibility that the observed mirror asymmetries are due — perhaps mostly due — to such wave function differences is an area of research that deserves more attention.

V. SUMMARY

Lifetimes of bound states in ^{15}N below the excitation energy of 9.1 MeV were surveyed by the DSA method through the inverse reaction ^{2}H(^{14}N, $p\gamma$) and by the GRID method through the thermal-neutron capture reaction ^{14}N(n, γ).

By using implanted targets in a high stopping-power medium (Au), the stopping power of which is experimentally known, and by simulating the slowing-down process with the Monte Carlo method, the lifetimes values (in fs) of 43 ± 4 (E_x = 5.30 MeV), 11 ± 2 (7.16 MeV), and 129 ± 6 (7.57 MeV) were obtained in the DSA measurements. Comparison of the line shapes obtained with Au (high stopping-power) and Si (low stopping-power) backings yielded the upper lifetime limits (in fs) of < 12 (E_x = 6.32 MeV), < 3 (7.30 MeV), < 3 (8.31 MeV), < 10 (8.57 MeV), and < 4 (9.05 MeV).

GRID measurements were made with melamine, silicon nitride, and air. The FWHM values of the Doppler-broadened γ-ray line shapes were simulated with a recently introduced molecular-dynamics simulation program of the slowing down of atoms recoiling at ultralow velocities. This analysis yielded the lifetime values (in fs) of 40 ± 3 (E_x = 5.30 MeV), < 2 (6.32 MeV), < 3 (7.30 MeV), and < 3 (8.31 MeV).

The recommended lifetime values (in fs) of 41 ± 3, 11 ± 2, and 129 ± 6 for the 5.30-, 7.16-, and 7.57-MeV levels, respectively, are believed to be more accurate and reliable than currently available in the literature.

Transition strengths for nine levels below excitation energies of ~ 9 MeV in ^{15}N and ^{15}O were compared

with the results of a shell-model calculation. The level of agreement between theory and experiment was generally rather good. In particular, the agreement for $M1$ strengths, together with an understanding of the wide variation in Coulomb-energy shifts for excited states, supported the basic shell-model description of the structure of low-lying, positive-parity states in terms of mixed $1p2h$ and $3p4h$ configurations. A breakdown of mirror symmetry was noted for $E1$ transition strengths, particularly in the ground-state transitions from the $\frac{1}{2}^+$ states. The conjecture that this breakdown could be primarily caused by differences in configuration mixing in ^{15}N and ^{15}O, which mixings are themselves a natural consequence of the differing Coulomb-energy shifts for different configurations, is worthy of further study.

Although the current measurements improve the precision with which three lifetimes are known in ^{15}N, the uncertainties in several others are large. For the 8.31-MeV, $\frac{1}{2}^+$ and 8.57-MeV, $\frac{3}{2}^+$ states, measurements of longitudinal (e,e') form factors at low momentum transfers might be particularly helpful. In ^{15}O, only upper limits are known on the lifetimes of the 6.18-MeV, $\frac{3}{2}^-$ and 6.79-MeV, $\frac{3}{2}^+$ states; the lifetimes should be around 0.3 fs (from scaling the ^{15}N lifetime by the ratio of theoretical $M1$ strengths) and 0.6 fs (from assuming mirror symmetry), respectively. Measurements, with relatively small uncertainties, of the four lifetimes identified above would (a) essentially complete the set of information on the transition strengths for low-lying states of ^{15}N and ^{15}O, (b) better quantify the breakdown of mirror symmetry for $E1$ transition strengths, and (c) provide a strong test of theoretical calculations, including the mechanisms for symmetry breaking.

ACKNOWLEDGMENTS

One of us (S.R.) acknowledges enlightening discussions with K. J. Wetzel concerning the earliest observations of Doppler broadening in the (thermal n, γ) reaction and on the importance of angular correlation effects in its interpretation. We thank S. J. Robinson for his invaluable suggestions concerning the convolution of simulated line shapes in the GRID analysis. The current work was sponsored in part by the Department of Energy under Contracts No. DE-AC05-85OR21400 with Martin Marietta Energy Systems, Inc. (Oak Ridge), No. W-7405-eng-36 with the University of California (Los Alamos), and No. DE-AC02-76-CH00016 with the Associated Universities, Inc. (Brookhaven), and in part by the Academy of Finland.

APPENDIX A: BRANCHING RATIOS FOR SELECTED ^{15}N LEVELS

The branching ratios given in Table 15.5 of Ref. [1] for the decay of the 8.31-, 8.57-, and 9.0-MeV levels of ^{15}N represent a particular selection from the three original Refs. [51–53] (tabulated in Table 15.10 of Ref. [54]) without an average being taken. Moreover, the branching ratios for a given level do not sum to 100%. An explanation of how we arrived at the branching ratios given in Table VI is given below.

The 8.31-MeV level. Reference [53] gives a 1.2(6)% branch to the 7.16-MeV level while Ref. [51] puts a limit of $< 1\%$ on this branch. Here, the 1.2% branch is ignored, because it would correspond to an implausible $E2$ strength, and the remaining branches are renormalized to sum to 100% and then averaged with the results of Ref. [51].

The 8.57-MeV level. In Ref. [1], the branches for the 6.32- and 7.16-MeV levels are taken from Ref. [53]. Here, the 3.6% branch to the 7.16-MeV level is taken from Ref. [44], the results of Refs. [51] and [52] are renormalized to take this branch into account, the results of Refs. [51] and [53] for the branch to the 6.32-MeV level are averaged, and all three results for the large branches are averaged.

The 9.05-MeV level. Reference [51] gives a 1.2(4)% branch to the 7.30-MeV level while Ref. [53] puts a limit of $< 1\%$ on branches to the three levels near 7.3 MeV. Here, the 1.2% branch is ignored, although it would correspond to a plausible $M1$ strength, and the remaining branches are renormalized to sum to 100% before averaging the results from all three references.

APPENDIX B: USE OF (e,e') AND (π,π') DATA

The (e,e') and (π,π') data that are used in the construction of Table VII are taken from several unpublished theses. The NIKHEF (e,e') data for the excitation of negative-parity states appear in the thesis of de Vries [55] and, for the positive-parity states, in the thesis of Salah [56], which also contains the earlier 180° UMass/Glasgow data from Bates. The LAMPF data for inelastic π^+ and π^- scattering at $T_\pi = 164$ MeV appear in the thesis of Saunders [57].

In the NIKHEF data, the 5.27- and 5.30-MeV levels are not resolved; they are separated by line shape fitting, while the 7.15- and 7.30-MeV levels are resolved. Longitudinal form factors for all the levels listed in Table VI have been obtained for momentum transfers in the range $0.6\ \text{fm}^{-1} < q_{\text{eff}} < 3.2\ \text{fm}^{-1}$.

The $B(E\lambda)$ values in Table VII were obtained by fitting the measured (e,e') form factors with polynomial times Gaussian expressions in the variable $y = (bq/2)^2$ (see Sec. V A of Ref. [47]), where b is the harmonic oscillator length parameter. The square of the leading term in the polynomial gives $B(E\lambda)\uparrow$ in units of $e^2\,\text{fm}^{2\lambda}$ ($E2$ W.u. $= 2.198\ e^2\,\text{fm}^4$, $E3$ W.u. $= 13.366\ e^2\,\text{fm}^6$). This is a model-dependent procedure when low-q data are not available. Nevertheless, experience shows that it is a rather reliable means of extracting $E2$ and $E3$ matrix elements in light nuclei. The uncertainties on the $B(E\lambda)$ values in columns 6 and 9 of Table VII are purely statistical, but some idea of the model dependence can be obtained by varying the parametrization; generally, such changes in the fitting procedure do not move the fitted $B(E\lambda)$ values outside the statistical error bars for other reasonably good fits.

Over the range of momentum transfers covered by the

NIKHEF data, the longitudinal form factors for positive-parity states with $J \leq \frac{7}{2}$ are all similar in shape (see Sec. V E 4 of Ref. [47]). Measurements at low q are needed to obtain information on $B(E1)$ values for excitation of the $\frac{1}{2}^+$ and $\frac{3}{2}^+$ states.

The older work of Kim *et al.* [17] has not been used here because the doublets at 5.3 MeV and 7.3 MeV are not resolved and because their analysis using Helm-model transition densities, which are surface peaked corresponding to giant-resonance-type transitions, is not appropriate for $E1$ transitions to low-lying excited states.

It is useful to define [47] amplitudes A_p and A_n as

$$A_p = (1 + \delta e_p)Z_p + \delta_n Z_n,$$
$$A_n = \delta e_n Z_p + (1 + \delta_p)Z_n, \tag{B1}$$

where $Z_{p/n}$ are shell-model one-body density matrices in the p/n representation and $\delta_{p/n}$ are effective charges. The $B(E\lambda)$ values for ^{15}N and ^{15}O are proportional to A_p^2 and A_n^2, respectively, and A_p values can be deduced from the measured $B(E\lambda)$ values for ^{15}N (see Table VII). To a reasonably good approximation, the pion inelastic scattering ratio R near resonance energies is given by

$$R = \frac{\sigma(\pi^+)}{\sigma(\pi^-)} = \left(\frac{3A_p + A_n}{3A_n + A_p}\right)^2, \tag{B2}$$

which can be used to obtain A_p/A_n. For strong $E2$ and $E3$ transitions, A_p/A_n is chosen to be positive because the isoscalar matrix element is expected to dominate. The ratios given in column 7 of Table VII were obtained by averaging the experimental ratios [57] of cross sections at five angles at 5° intervals around the peak cross section. The uncertainties in the $B(E\lambda)$ values for ^{15}O are dominated by the uncertainty in R, except for the $\frac{5}{2}^+_1$ state for which uncertainties in the (e, e') form factor are relatively large as a consequence of the line shape fitting required to separate the cross sections for the 5.27- and 5.30-MeV levels of ^{15}N. Apart from the model dependence inherent in Eq. (B2), there is also the possibility that multipoles other than the dominant one contribute to the pion cross sections. In fact, the cross section for the 7.16-MeV level is clearly dominated by the $M2$ multipole. In the other cases, the cross sections have the shapes expected for the dominant multipole. The 5.27- and 5.30-MeV levels are not resolved, and the 5.30-MeV level is expected to contribute, especially at small angles, with a peak cross section which is about 10% of that of the 5.27-MeV level.

[1] F. Ajzenberg-Selove, Nucl. Phys. **A523**, 1 (1991).

[2] P. G. Bizzeti, A. M. Bizzeti-Sona, S. Kalbitzer, and B. Povh, Nucl. Phys. **A104**, 577 (1967).

[3] M. Forterre, J. Gerber, J. P. Vivien, M. D. Goldberg, K.-H. Speidel, and P. N. Tandon, Phys. Rev. C **11**, 1976 (1975).

[4] H. P. Seiler, R. Kulessa, P. M. Cockburn, P. Marmier, and P. H. Barker, Nucl. Phys. **A241**, 159 (1975).

[5] J. Billowes, J. Burde, J. A. G. De Raedt, M. A. Grace, W. R. Kölbl, and A. Pakou, J. Phys. G **9**, 1407 (1983).

[6] T. K. Alexander, A. E. Litherland, and C. Broude, Can. J. Phys. **43**, 2310 (1965).

[7] K. J. Wetzel, Phys. Rev. **181**, 1465 (1969).

[8] R. D. Gill, J. S. Lopes, O. Häusser, and H. J. Rose, Nucl. Phys. **A121**, 209 (1968).

[9] L. H. Harwood and K. W. Kemper, Phys. Rev. C **20**, 1383 (1979).

[10] G. A. Beer, P. Brix, H.-G. Clerc, and B. Laube, Phys. Lett. **26B**, 506 (1968).

[11] J. C. Kim, H. S. Caplan, and I. P. Auer, Phys. Lett. **56B**, 442 (1975).

[12] R. Moreh and O. Shahal, Nucl. Phys. **A252**, 429 (1975).

[13] R. Moreh, O. Shahal, and V. Volterra, Nucl. Phys. **A262**, 221 (1976).

[14] R. Moreh, W. C. Sellyey, and R. Vodhanel, Phys. Rev. C **23**, 988 (1981).

[15] K. P. Lieb, Nucl. Phys. **85**, 461 (1966).

[16] P. M. Cockburn, R. W. Krone, and H. E. Siefken, Bull. Am. Phys. Soc. **13**, 1423 (1968).

[17] J. C. Kim, H. S. Caplan, and J. C. Bergstrom, Nucl. Phys. **A246**, 282 (1975).

[18] The improvements involve (a) implanted targets in high stopping-power media whose stopping powers are experimentally known and (b) computer simulations of the slowing-down process and experimental conditions with the Monte Carlo method. For further details, see P. Tikkanen, J. Keinonen, A. Kuronen, A. Z. Kiss, E. Koltay, E. Pintye, and B. H. Wildenthal, Nucl. Phys. **A517**, 176 (1990).

[19] E. C. Campbell, J. A. Harvey, and G. G. Slaughter, Bull. Am. Phys. Soc. **13**, 1423 (1968).

[20] The new term GRID was coined by Börner. At Grenoble, he and his colleagues are using this method and a crystal spectrometer to systematically measure short lifetimes in heavy nuclides. See for instance, Refs. [38] and [21]. In a variation of the GRID method, the lifetime of a level populated in (n, γ) reaction can also be deduced from the small energy shift that might be measured, in favorable cases, from $\gamma\gamma$-coincidence (NaI-Ge) spectra obtained at 90° and 180°. This method is in use at the Kiev reactor to study light nuclides. See Yu. E. Koshutskii, V. T. Kupryashkin, N. V. Stril'chuck, A. I. Feoktistov, and I. P. Shapovalova, Izv. Akad. Nauk. SSSR, Ser. Fiz. **53**, 2125 (1989); **54**, 844 (1990); V. T. Kupryashkin, V. S. Oleinik, N. V. Stril'chuck, A. I. Feoktistov, and I. P. Shapovalova, *ibid.* **54**, 846 (1990); V. T. Kupryashkin, N. V. Stril'chuck, A. I. Feoktistov, and I. P. Shapovalova, *ibid.* **54**, 2145 (1990); N. S. Kravets, V. T. Kupryashkin, N. V. Stril'chuck, A. I. Feoktistov, and I. P. Shapovalova, *ibid.* **54**, 2162 (1990).

[21] A. Kuronen, J. Keinonen, H. G. Börner, J. Jolie, and S. Ulbig, Nucl. Phys. **A549**, 59 (1992).

[22] J. Keinonen, A. Kuronen, P. Tikkanen, H. G. Börner, J. Jolie, S. Ulbig, E. G. Kessler, R. M. Nieminen, M. J.

Puska, and A. P. Seitsonen, Phys. Rev. Lett. **67**, 3692 (1991).
[23] J. Keinonen, V. Karttunen, J. Räisänen, F.-J. Bergmeister, A. Luukkainen, and P. Tikkanen, Phys. Rev. B **34**, 8981 (1986).
[24] A. Kehrel, J. Keinonen, P. Haussalo, K. P. Lieb, and M. Uhrmacher, Radiat. Eff. Defects **118**, 297 (1991).
[25] A. S. Soltan, R. Vassen, and P. Jung, J. Appl. Phys. **70**, 793 (1991).
[26] W. H. Trzaska, Nucl. Instrum. Methods A **297**, 223 (1990).
[27] S. Raman, R. F. Carlton, J. C. Wells, E. T. Jurney, and J. E. Lynn, Phys. Rev. C **32**, 18 (1985).
[28] J. Keinonen, M. Bister, and A. Anttila, Nucl. Phys. **A286**, 505 (1977).
[29] A. Kuronen, J. Räisänen, J. Keinonen, P. Tikkanen, and E. Rauhala, Nucl. Instrum. Methods B **35**, 1 (1988).
[30] J. F. Ziegler, J. P. Biersack, and U. Littmark, in *The Stopping and Range of Ions in Solids*, edited by J. F. Ziegler (Pergamon, New York, 1985), Vol. 1.
[31] P. Tikkanen, J. Keinonen, A. Kuronen, A. Z. Kiss, E. Koltay, E. Pintye, and B. H. Wildenthal, Nucl. Phys. **A517**, 176 (1990).
[32] J. Keinonen, A. Luukkainen, A. Anttila, and M. Erola, Nucl. Instrum. Methods **216**, 249 (1983).
[33] J. Keinonen, in *Capture Gamma-Ray Spectroscopy and Related Topics (Holiday Inn—World's Fair, Knoxville, Tennessee)*, Proceedings of the Fifth International Symposium on Capture Gamma-Ray Spectroscopy and Related Topics, edited by S. Raman, AIP Conf. Proc. No. 125 (AIP, New York, 1984), p. 557.
[34] P. Tikkanen, J. Keinonen, V. Karttunen, and A. Kuronen, Nucl. Phys. **A456**, 337 (1986).
[35] P. Tikkanen, J. Keinonen, A. Kangasmäki, Zs. Fülöp, A. Z. Kiss, and E. Somorjai, Phys. Rev. C **43**, 2162 (1991).
[36] Another favorable case is ^{11}B, which also has been studied by Wetzel, Phys. Rev. **186**, 1292 (1969). Such favorable cases are very limited because the successful observation of Doppler broadening with Ge detectors requires both a light nucleus and a large neutron separation energy.
[37] D. Janssen, J. Jolie, and H. G. Börner, Z. Phys. B **88**, 63 (1992).
[38] H. G. Börner and J. Jolie, J. Phys. G **19**, 217 (1993).
[39] K. Palmö (private communication).
[40] *Handbook of Chemistry and Physics*, edited by R. C. Weast, M. J. Astle, and W. H. Beyer (CRC Press, Boca Raton, FL, 1983).
[41] R. Marchard, Y. Laurent, J. Lang, and M. T. Le Bihan, Acta Crystallogr. B **25**, 2157 (1969).
[42] I. M. Torrens, *Interatomic Potentials* (Academic Press, New York, 1972).
[43] *The Electromagnetic Interaction in Nuclear Spectroscopy*, edited by W. D. Hamilton (North-Holland, Amsterdam, 1975).
[44] U. Schröder, H. W. Becker, G. Bogaert, J. Görres, C. Rolfs, H. P. Trautvetter, R. E. Azuma, C. Campbell, J. D. King, and J. Vise, Nucl. Phys. **A467**, 240 (1987).
[45] S. J. Skorka, J. Hertel, and T. W. Retz-Schmidt, Nucl. Data A **2**, 347 (1966).
[46] D. E. Alburger and D. J. Millener, Phys. Rev. C **20**, 1891 (1979).
[47] D. J. Millener, D. I. Sober, H. Crannell, J. T. O'Brien, L. W. Fagg, S. Kowalski, C. F. Williamson, and L. Lapikás, Phys. Rev. C **39**, 14 (1989).
[48] I. S. Towner and F. C. Khanna, Nucl. Phys. **A399**, 334 (1983).
[49] D. J. Millener, J. W. Olness, E. K. Warburton, and S. S. Hanna, Phys. Rev. C **28**, 497 (1983).
[50] D. Kurath, Phys. Rev. Lett. **35**, 1546 (1975).
[51] E. K. Warburton, J. W. Olness, and D. E. Alburger, Phys. Rev. **140**, B1202 (1965).
[52] E. K. Warburton and J. W. Olness, Phys. Rev. **147**, 698 (1966).
[53] G. W. Phillips, F. C. Young, and J. B. Marion, Phys. Rev. **159**, 891 (1967).
[54] F. Ajzenberg-Selove, Nucl. Phys. **A152**, 1 (1970).
[55] J. W. de Vries, Ph.D. thesis, University of Utrecht, 1987 (unpublished).
[56] S. A. Salah, Ph.D. thesis, University of Glasgow, 1987 (unpublished).
[57] D. P. Saunders, Ph.D. thesis, University of Texas at Austin, 1991 (unpublished).

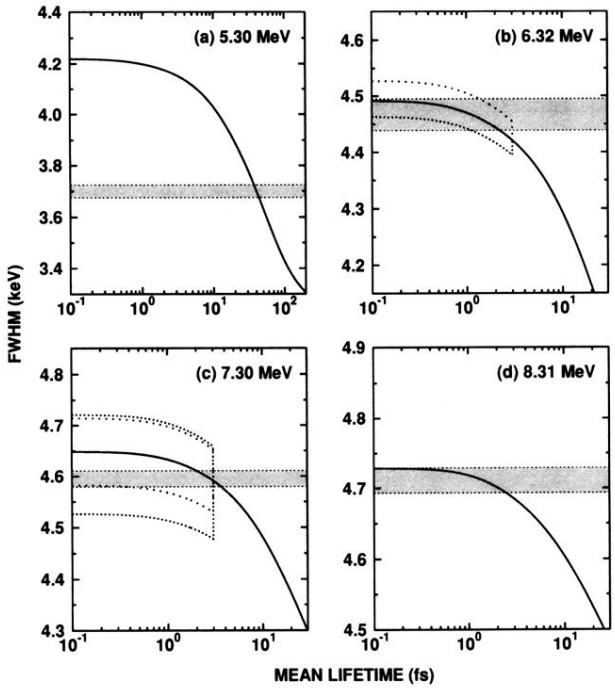

FIG. 6. Calculated FWHM values of four secondary transitions as a function of the level lifetimes. The recoiling nuclei are slowing down in melamine. The solid line corresponds to zero angular correlation. The measured FWHM value is shown by the shaded band. In the cases of the 5.30- and 8.31-MeV transitions, the measured FWHM values lead directly to lifetime values because angular correlation is not a factor in either case. In the cases of the 6.32- and 7.30-MeV transitions, their known mixing ratios together with the additional assumptions restrict the calculated FWHM values to the dotted region, as shown in (b) and (c), respectively. The spin sequences and the mixing ratios are discussed in Sec. III B 2.